



Cite this: DOI: 10.1039/c6cp01964a

Ruthenium and ruthenium oxide nanofiber supports for enhanced activity of platinum electrocatalysts in the methanol oxidation reaction†

Geon-Hyoung An,^a Eun-Hwan Lee^b and Hyo-Jin Ahn^{*ab}

Novel supports for the dispersion of Pt electrocatalysts in fuel cells are constantly being developed in order to improve the electrochemical performance and reduce the cost. The electrocatalytic activity and stability in fuel cells largely depend on the surface morphology and structure of the support. In this study, Ru and RuO₂ nanofibers prepared by electrospinning and post-calcination have been considered as Pt-catalyst supports. The composite material loaded with 20 wt% Pt catalyst exhibited a high anodic current density of 641.7 mA mg_{Pt}⁻¹, a high *I*_F/*I*_B ratio of 1.9, and excellent electrocatalytic stability compared to commercial Pt/C. The improved anodic current density of the composite is attributed to the high dispersion of the Pt catalyst over the large surface area of the nanosized support grains, while its low onset potential, high *I*_F/*I*_B ratio, and excellent electrocatalytic stability are ascribed to a bifunctional effect resulting from the existence of Ru atoms on the support surface. Finally, the efficient electron transfer and a rapid diffusion rate of the electrolyte are due to the unique network structure of the supports. Thus, the Ru and RuO₂ nanofiber composites act as promising Pt-catalyst supports for the methanol oxidation reaction.

Received 24th March 2016,
Accepted 2nd May 2016

DOI: 10.1039/c6cp01964a

www.rsc.org/pccp

Introduction

As environmental pollution and the depletion of fossil fuels are becoming increasingly serious problems, the development of new clean energy technologies is imperative. A fuel cell is an electrochemical energy device that converts chemical energy from a fuel to electrical energy by means of a chemical reaction.^{1–3} Among the different types of fuel cells, direct methanol fuel cells (DMFCs) are widely applied in portable electrical devices and electric vehicles because of their high energy density, high energy conversion efficiency, low operating temperature, ease of storage and transport (compared to hydrogen fuel cells), and low emission of pollutants.^{4–6} DMFCs consist of four main components: the anode, cathode, membrane, and electrolyte. The methanol oxidation reaction (MOR) takes place on the electrocatalysts of the anode, which are usually the main factors determining the electrochemical activity and cost of DMFCs. The use of Pt electrocatalysts has several serious disadvantages such as their high-cost, tendency to agglomerate, and poor CO tolerance,

owing to the accumulation of surface-adsorbed intermediate carbonaceous species such as CO, COOH, and CHO. These disadvantages may hamper the commercialization of DMFCs.^{7–11}

To overcome these problems, much research effort has been devoted to nanosized Pt electrocatalysts, Pt-metal alloys, and the use of catalyst supports.^{12–14} Of these strategies, the introduction of supports such as carbon, metal/metal oxides, and carbide is an effective technique to minimize the loading of Pt electrocatalysts and improve their electrocatalytic activity and stability in DMFCs.^{15–20} Currently, commercial DMFC technology generally employs carbon-based supports for Pt electrocatalysts because of their high surface area and high electrical conductivity. However, corrosion, poor CO tolerance, and dissolution of Pt electrocatalysts are still unresolved issues with the use of carbon-based supports, causing rapid decay of the electrocatalytic activity and stability.^{21–23} Thus, the development of novel supports is the key for the development of high-efficiency DMFCs.

Metal and metal oxides have also been used as supports owing to their excellent electrocatalytic stability, CO tolerance, and physicochemical properties.^{24–32} More importantly, high-surface-area supports are beneficial for the dispersion of Pt electrocatalysts and improved electrocatalytic activity.^{29–32} Among the possible candidates for metal and metal oxide supports (*e.g.*, TiO₂, SiO₂, WO₃, and ZnO), Ru and RuO₂ are particularly attractive due to their high electrical conductivity and excellent electrochemical stability over a wide potential range.^{12–14,33–36}

^a Program of Materials Science & Engineering, Convergence Institute of Biomedical Engineering and Biomaterials, Seoul National University of Science and Technology, Seoul 139-743, Korea. E-mail: hjahn@seoultech.ac.kr; Fax: +82-2-973-6657; Tel: +82-2-970-6622

^b Department of Materials Science and Engineering, Seoul National University of Science and Technology, Seoul 139-743, Korea

† Electronic supplementary information (ESI) available. See DOI: 10.1039/c6cp01964a

Furthermore, Ru and RuO₂ exhibit good CO tolerance in the MOR, which is attributed to the existence of Ru–OH bonds at their surfaces (termed the bifunctional effect) imparting improved electrocatalytic activity and stability.^{33–36} In addition, one-dimensional structures are known to exhibit improved electron transfer and efficient electrolyte diffusion in electrochemical devices such as secondary batteries, electrochemical capacitors, and fuel cells.^{13,14} For DMFCs, a network consisting of one-dimensional supports is considered to be the ideal support structure for Pt electrocatalysts owing to the efficient electron transfer and a rapid diffusion rate of the electrolyte.^{37,38} Thus, some different strategies have been tried to develop one-dimensional RuO₂ supports for improvement of the MOR. For example, Gu *et al.*³⁹ fabricated Pt electrocatalysts dispersed on RuO₂ nanorods for the MOR, indicating increased catalytic activity. Yeom *et al.*⁴⁰ synthesized electro-spun RuO₂ nanofiber supported Pt electrocatalysts and reported superior electrocatalytic activities. These research studies include the large-sized grains (over ~70 nm) of the supports having a low surface area, resulting in poor dispersion of Pt electrocatalysts. However, novel architectures like well-dispersed Pt electrocatalysts on the Ru and RuO₂ nanofiber supports with nanosized grains, which were fabricated by electrospinning and post-calcination, have not yet been studied. Furthermore, we prepared Ru and RuO₂ nanofiber supports at three different temperatures (300, 400, and 500 °C) in order to obtain an optimized support.

Experimental

Chemicals

Polyacrylonitrile (PAN, $M_w = 150\,000$), ruthenium(III) chloride hydrate (RuCl₃·*x*H₂O), *N,N*-dimethylformamide (DMF), chloroplatinic acid hydrate (H₂PtCl₆·*x*H₂O, ≥99.9%), sodium borohydride (NaBH₄), Nafion perfluorinated resin solution, 2-propanol, methanol (anhydrous, 99.8%), and sulfuric acid (H₂SO₄, ACS reagent, 70%) were purchased from Sigma-Aldrich. All chemicals were used without further purification.

Synthesis of Pt catalyst/Ru and RuO₂ nanofiber composites

Pt catalyst/Ru and RuO₂ nanofiber composites were synthesized using sequential electrospinning, post-calcination, and reduction. First, to synthesize Ru nanoparticle-embedded carbon nanofibers, 10 wt% PAN and 3 wt% RuCl₃·*x*H₂O were dissolved in DMF with vigorous stirring for 5 h. Electrospinning was performed at a feeding rate of 0.03 mL h⁻¹ and a voltage of *ca.* 13 kV. The distance between the 23-gauge needle and the collector was set at 15 cm under 10% humidity. The as-spun nanofibers were stabilized at 280 °C for 2 h in air and then carbonized at 800 °C for 2 h under N₂ gas (99.999%). To control the grain size of the supports, the Ru nanoparticle-embedded carbon nanofibers were calcined in air using a box furnace at 300, 400, or 500 °C for 30 min. Then, a reduction method was employed to prepare the Pt electrocatalysts on Ru and RuO₂ nanofiber composites (hereafter referred to as Pt/Ru–RuO₂). The Ru and RuO₂ nanofiber composites were dispersed in deionised (DI) water with stirring

and then 0.56 mM H₂PtCl₆·*x*H₂O was added. A NaBH₄ solution (100 mg mL⁻¹) was used as a reducing agent for depositing 20 wt% metallic Pt electrocatalysts onto the supports.^{9,23} In the reduction process, a NaBH₄ solution was quickly poured into the prepared solution under stirring to reduce the Pt precursor for 1 h at 20 °C. The resultant samples were washed several times with DI water and freeze-dried at –50 °C to acquire the metallic Pt phases. Thus, we obtained Pt/Ru–RuO₂ at 300, 400, and 500 °C (herein designated as Pt/Ru–RuO₂ 300, Pt/Ru–RuO₂ 400, and Pt/Ru–RuO₂ 500, respectively). The Pt catalyst/Ru nanoparticle-embedded carbon nanofiber precursor (hereafter referred to as Pt/Ru–CNFs) was used for comparison.

Characterization

The morphologies and structures of the composites were investigated by field-emission scanning electron microscopy (FESEM; Hitachi S-4800) and transmission electron microscopy (MULTI/TEM; Tecnai G², KBSI Gwangju Center). Surface properties such as specific surface area, total pore volume, and average pore diameter were characterized by the Brunauer–Emmett–Teller (BET) method using N₂ adsorption at 77 K. To investigate the distribution of elements in the samples, TEM-EDS mapping was observed using a Phillips CM20T/STEM equipped with an energy-dispersive X-ray spectrometer (EDS). The crystal structures and chemical bonding states were characterized by X-ray diffractometry (XRD, Rigaku D/MAX2500 V) in the range of 10°–90° with a step size of 0.02°, and X-ray photoelectron spectroscopy (XPS, ESCALAB 250) with an Al K α X-ray source. The binding energies of the XPS spectra were standardized to the C 1s core level (284.5 eV).

Electrochemical characterization

All electrochemical measurements were performed using an Eco Chemie Autolab PGSTAT302N potentiostat/galvanostat with a conventional three-electrode system consisting of a glassy carbon electrode as a working electrode (0.0706 cm²), a Pt wire as a counter electrode, and a Ag/AgCl reference electrode (saturated KCl). For the catalyst inks, 10 mg of the catalyst powder was ultrasonically dispersed in 900 μ l of 2-propanol and DI water containing 5 wt% Nafion solution until a dark homogeneous dispersion was achieved. Then, the catalyst inks were carefully dropped onto a glassy carbon electrode to give a Pt catalyst loading of around 35 μ g cm⁻² and it was dried at room temperature. The electrochemical surface area (ECSA) was measured using cyclic voltammetry (CV) measurements of the hydrogen adsorption/desorption area in a 0.5 M H₂SO₄ electrolyte between –0.2 and 1.0 V (*vs.* Ag/AgCl) at a scan rate of 50 mV s⁻¹. The methanol oxidation tests were performed in a 2 M CH₃OH and 0.5 M H₂SO₄ electrolyte between –0.2 and 1.0 V (*vs.* Ag/AgCl) at a scan rate of 50 mV s⁻¹. To examine the electrocatalytic stability, chronoamperometry (CA) was conducted in a 2 M CH₃OH and 0.5 M H₂SO₄ electrolyte at a constant potential of 0.5 V for 2000 s. Before all electrochemical tests, the electrolyte was purged with high-purity Ar gas to expel oxygen. For comparison, electrochemical measurements of commercial Pt/C (20 wt% Pt on Vulcan XC-72R) were also conducted under the same conditions.

Results and discussion

Fig. 1 schematically illustrates the synthetic process for fabricating Pt/Ru–RuO₂ 400. As shown in Fig. 1a, the nanofiber material comprising PAN and RuCl₃ was prepared by electrospinning, and then carbonized in N₂ to obtain Ru nanoparticle-embedded CNFs (Fig. 1b). To obtain the unique surface of the supports, the Ru nanoparticle-embedded CNFs were calcined at 400 °C for 30 min, removing the carbon and converting the Ru nanoparticles in the CNF matrix to Ru and RuO₂ nanofibers (Fig. 1c). Finally, Pt/Ru–RuO₂ 400 was synthesized by a reduction method, which deposited the well-dispersed Pt electrocatalysts onto the Ru and RuO₂ nanofiber supports (Fig. 1d).

Fig. 2 shows the low-resolution (Fig. 2a–d) and high-resolution (Fig. 2e–h) FESEM images of Pt/Ru–CNFs, Pt/Ru–RuO₂ 300, Pt/Ru–RuO₂ 400, and Pt/Ru–RuO₂ 500. All samples indicate that the interconnected network structures will afford efficient electron transfer and a rapid diffusion of the electrolyte during the MOR. The diameters of the samples are estimated to be *ca.* 315–345 nm for Pt/Ru–CNFs (Fig. 2a and e), 187–213 nm for Pt/Ru–RuO₂ 300 (Fig. 2b and f), 163–203 nm for Pt/Ru–RuO₂ 400 (Fig. 2c and g), and 183–207 nm for Pt/Ru–RuO₂ 500 (Fig. 2d and h). After post-calcination, Pt/Ru–RuO₂ 300, 400, and 500 become smaller in diameter than Pt/Ru–CNFs. This is because the CNF matrix is removed by post-calcination by the oxidation reaction between carbon and oxygen, as indicated in Fig. S1 (ESI[†]). Following post-calcination, we observe a noticeable change in the surface morphology of the Ru and RuO₂ nanofiber supports. The supports become nanosized grains with porous structures following treatment at 300 and 400 °C, as shown in Fig. S2 (ESI[†]). After reduction, Pt/Ru–CNFs (Fig. 2a and e) exhibit large agglomerated Pt catalyst particles on the surface due to strong carbon–carbon bonds at the edges of the Ru–CNF supports.^{9,23} For Pt/Ru–RuO₂ 300 (Fig. 2b and f), fewer agglomerated Pt electrocatalysts are observed on the supports due to the carbon layer on the Ru and RuO₂ surface, as shown in the TEM images. Furthermore,

Pt/Ru–RuO₂ 400 (Fig. 2c and g) exhibits no agglomeration of the Pt catalyst, indicating efficient dispersion of Pt particles on the support. These results are attributed to the porosity of the support, which affords numerous accessible platforms for the nanosized Pt particles and simultaneously improves the interaction between the Pt catalyst and the support. Therefore, post-calcination could successfully remove the CNF matrix by the oxidation reaction between carbon and oxygen and then Ru was oxidized to RuO₂. The existence of oxygen phases in RuO₂ could provide large anchoring sites for Pt electrocatalysts, resulting in well-dispersed Pt electrocatalysts on the support surface.²⁶ Accordingly, post-calcination is essential to obtain optimized supports with well-dispersed Pt electrocatalysts on the support surface for enhanced activity of Pt electrocatalysts in the methanol oxidation reaction.^{41,42} However, Pt/Ru–RuO₂ 500 (Fig. 2d and h) exhibits large agglomerated particles of Pt catalyst (61–81 nm) on the angled surface of the supports, implying the presence of less accessible platforms for the Pt catalyst. Therefore, the SEM results suggest that the post-calcination temperature plays an important role in determining the surface properties of the supports as well as the dispersion of the Pt catalyst particles on the supports. The dispersion and distribution of the Pt catalyst on the supports was further observed using TEM, HRTEM, and TEM-mapping. Fig. 3 shows low-resolution (Fig. 3a–d) and high-resolution (Fig. 3e–h) TEM images of Pt/Ru–CNFs, Pt/Ru–RuO₂ 300, Pt/Ru–RuO₂ 400, and Pt/Ru–RuO₂ 500. Pt/Ru–CNFs exhibit large agglomerated Pt catalyst particles sparsely distributed on the support surface (Fig. 3a). In addition, Fig. 3e shows the nonuniformity contrast of the supports due to the existence of Ru nanoparticles (1–2 nm) in the CNF matrix. The Pt catalyst shows better dispersion in Pt/Ru–RuO₂ 300 than in Pt/Ru–CNFs. However, Pt/Ru–RuO₂ 300 exhibits a thin carbon layer (*ca.* 1.5 nm) on the Ru and RuO₂ surface, indicating that carbon is not completely removed owing to the relatively low post-calcination temperature (300 °C) (Fig. 3f). The thin carbon layer may interrupt the dispersion of the Pt catalyst owing to the strong carbon–carbon bonding at the edge surface.^{9,23} Noticeably, the images of Pt/Ru–RuO₂ 400 (Fig. 3c and g) show that the Pt catalyst particles are well dispersed on the support, and show no agglomeration. Here, the average grain size of the support is measured to be 7–9 nm. The formation of nanosized grains of the porous supports is ascribed to the removal of the CNF matrix and grain growth induced by Ostwald ripening processes during post-calcination.⁴³ Therefore, the excellent dispersion of the Pt catalyst in Pt/Ru–RuO₂ 400 is attributed to the porosity of the nanosized support grains, which exhibit a high surface area of 54.7 m² g^{−1}. This is significantly higher than that of the support in Pt/Ru–RuO₂ 500 (21.3 m² g^{−1}), as shown in Fig. S3 and Table S1 (ESI[†]). The high-resolution TEM image of Pt/Ru–RuO₂ 400 (Fig. 3g) shows the nanosized Pt catalyst particles (1–2 nm) and clear lattice fringes with a spacing of 0.22 nm, which are attributed to the (111) planes of Pt.^{43–45} However, for Pt/Ru–RuO₂ 500 (Fig. 3h), larger Pt catalyst particles (3–5 nm) are densely located on the support. The increased size of the Pt electrocatalysts is due to Ostwald ripening, which occurs due to the larger grain size and low surface area of the supports.

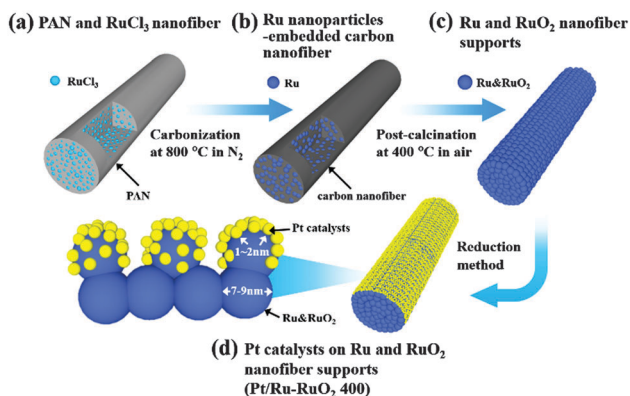


Fig. 1 Schematic illustration of synthetic routes for Pt/Ru–RuO₂-400. (a) PAN and RuCl₃ nanofibers fabricated by electrospinning. (b) Ru nanoparticle-embedded CNFs prepared by carbonization at 800 °C for 2 h in N₂. (c) Ru and RuO₂ composites obtained through post-calcination at 400 °C for 30 min in air. (d) Pt/Ru–RuO₂ 400 fabricated by a reduction method.

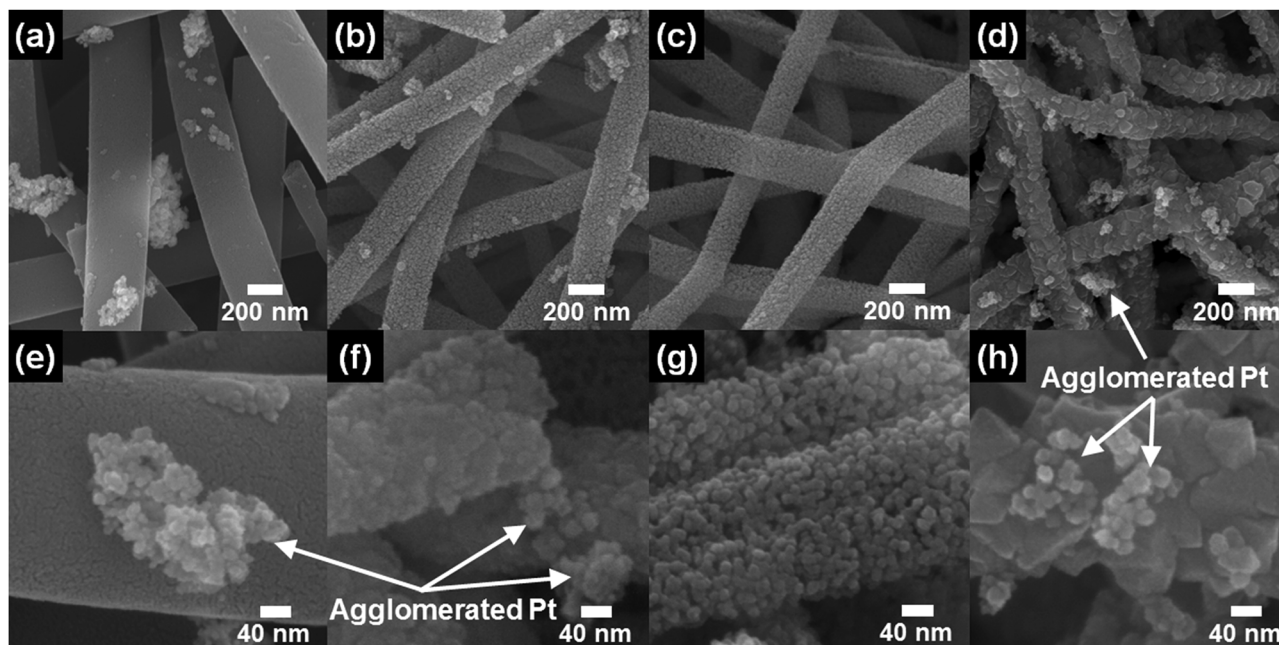


Fig. 2 (a–d) Low-resolution and (e–h) high-resolution FESEM images of (a and e) Pt/Ru–CNFs, (b and f) Pt/Ru–RuO₂ 300, (c and g) Pt/Ru–RuO₂ 400, and (d and h) Pt/Ru–RuO₂ 500.

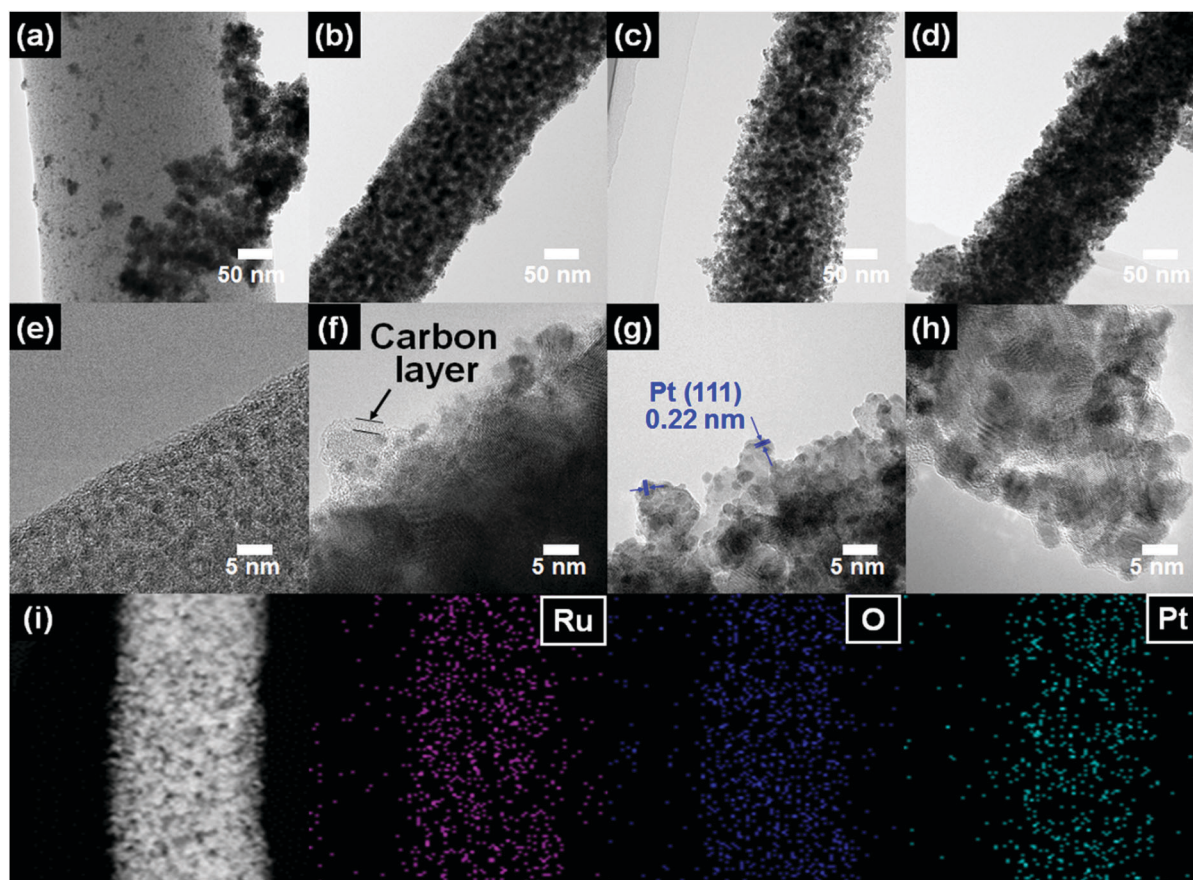


Fig. 3 (a–d) Low-resolution and (e–h) high-resolution TEM images of (a and e) Pt/Ru–CNFs, (b and f) Pt/Ru–RuO₂ 300, (c and g) Pt/Ru–RuO₂ 400, and (d and h) Pt/Ru–RuO₂ 500. (i) TEM-EDS mapping data of Pt/Ru–RuO₂ 400.

To further investigate the distribution of Ru, O, and Pt atoms of Pt/Ru–RuO₂ 400, TEM-EDS mapping was performed, as shown in Fig. 3i. The EDS results confirm that Ru and O atoms are uniformly dispersed along the nanofibers, indicating that RuO₂ is uniformly synthesized. In addition, the EDS results confirm that Pt atoms are uniformly located along the nanofibers, which indicates the efficient dispersion of the Pt catalyst on the support.

Fig. 4a shows the XRD patterns of the samples, which were obtained in order to investigate their crystalline phases and crystallinities. It is clearly confirmed by XRD measurements that some Ru phase in the CNFs is oxidized to RuO₂ during post-calcination, as observed in Fig. S4 (ESI[†]). Pt/Ru–CNFs present a broad peak at around 25° corresponding to the (002) layers of graphite, and diffraction peaks at 39.7°, 46.2°, 67.5°, and 81.3° corresponding to the (111), (200), (220), and (311) crystal planes, respectively, of Pt with a face-centred cubic structure (space group *Fm3m* [225]) (JCPDS card No. 04-0802). Furthermore, the diffraction peaks for Ru are hidden due to nanosized Ru in the CNF matrix, as shown in Fig. S4 (ESI[†]). In the case of Pt/Ru–RuO₂ 300, 400, and 500, the diffraction peaks indicate mixed phases composed of Ru and RuO₂. The diffraction peak for the Ru phase is observed at 44.0° corresponding to the (101) plane. The diffraction peaks of the RuO₂ phase are observed at 28.0°, 35.1°, 40.1°, and 54.3°, corresponding to the (110), (101), (200), and (211) planes, respectively. Furthermore, as the post-calcination temperature increases, the intensities of the diffraction peaks presented by the Ru phase decrease gradually, whereas the intensity of the diffraction peaks presented by the RuO₂ phase increases. The main diffraction peak of Pt at 39.7° was overlapped with the diffraction peak of RuO₂ at 40.1°, as shown in Fig. S5 (ESI[†]). Furthermore, the diffraction peaks presented by Pt are obscured by those of Ru and RuO₂ because of the much small quantity of nanosized Pt. Thus, we carried out XPS analysis after post-calcination to observe the existence of Pt.

To investigate the surface chemical bonding states, XPS measurements were performed, as shown in Fig. 4b and Fig. S6 (ESI[†]).

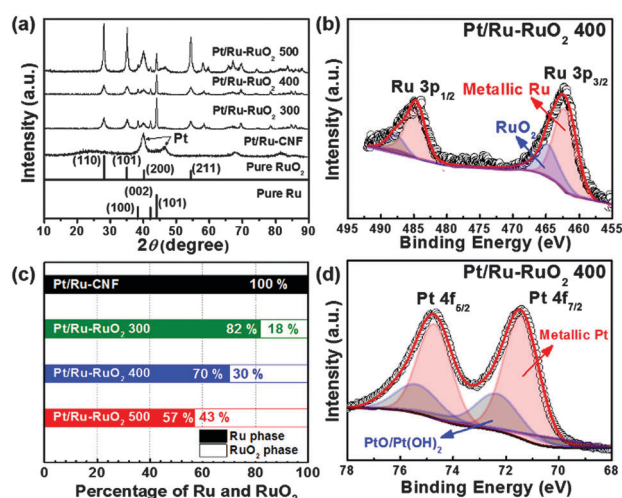


Fig. 4 (a) XRD patterns of Pt/Ru–CNFs, Pt/Ru–RuO₂ 300, Pt/Ru–RuO₂ 400, and Pt/Ru–RuO₂ 500. (b) Ru 3p core-level XPS spectra of Pt/Ru–RuO₂ 400. (c) Percentage of Ru and RuO₂ phases in the XPS spectra of Ru 3p. (d) XPS spectra from the Pt 4f_{7/2} and Pt 4f_{5/2} photoelectrons of Pt/Ru–RuO₂ 400.

Two pairs of doublets for Ru 3p_{3/2} and Ru 3p_{1/2} photoelectrons are observed in the Ru 3p core-level spectra of Pt/Ru–RuO₂ 400 (Fig. 4b). The lower-energy peaks (462.0 and 484.6 eV) are assigned to metallic Ru, while the higher-energy peaks (464.6 and 487.6 eV) are assigned to RuO₂.^{9,46} As the post-calcination temperature increases, the RuO₂ content gradually increases from 0 wt% (Pt/Ru–CNFs) to 18 wt% (Pt/Ru–RuO₂ 300), 30 wt% (Pt/Ru–RuO₂ 400), and 43 wt% (Pt/Ru–RuO₂ 500), as shown in Fig. 4c and Fig. S6 (ESI[†]). Moreover, the Pt 4f_{7/2} and Pt 4f_{5/2} photoelectrons are observed in the Pt 4f core-level spectra of Pt/Ru–RuO₂ 400 (Fig. 4d) at ca. 71.3 eV and ca. 74.7 eV, respectively, corresponding to metallic Pt.^{18,47} The small doublet at 72.3 and 75.4 eV can be assigned to oxidized Pt species such as PtO and Pt(OH)₂ due to the oxidization of Pt by O₂ and water vapour in the air.²⁶

Fig. 5a shows the CVs in an Ar-saturated 0.5 M H₂SO₄ electrolyte between –0.2 and 1.0 V (vs. Ag/AgCl) at a scan rate of 50 mV s^{–1}. CV curves typical of Pt electrocatalysts, with hydrogen adsorption/desorption peaks and oxidation/reduction peaks in agreement with previous studies, are exhibited for all the electrocatalysts, which means that all of them exhibit electrocatalytic activity depending on their ECSA.^{48,49} The number of catalytically active sites during the electrochemical reaction is determined by the ECSA, as shown in Fig. 5b. The ECSA value provides significant information related to the number of catalytically active sites per mass (g) of the catalyst, and is an essential parameter for comparing different electrocatalysts. The ECSA can be calculated using the following equation: ECSA (m² g^{–1}) = Q_H/([Pt] × 0.21)^{–1}, where Q_H is the charge for hydrogen desorption (mC cm^{–2}), [Pt] is the Pt loading (mg) on the electrode, and 0.21 is the charge required to oxidize a monolayer of H₂ on a clean Pt surface (mC cm^{–2}).^{48,49} The ECSAs of commercial Pt/C, Pt/Ru–CNFs, Pt/Ru–RuO₂ 300, Pt/Ru–RuO₂ 400, and Pt/Ru–RuO₂ 500 are calculated to be 53.6, 18, 75.2, 115.4, and 62.9 m² g_{Pt}^{–1}, respectively, suggesting that Pt/Ru–RuO₂ 400 presents more electrochemically

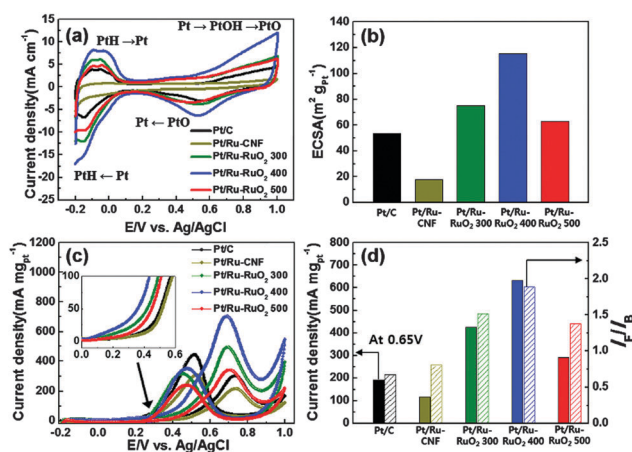


Fig. 5 Comparison of the electrocatalytic activity of commercial Pt/C, Pt/Ru–CNFs, Pt/Ru–RuO₂ 300, Pt/Ru–RuO₂ 400, and Pt/Ru–RuO₂ 500. (a) Cyclic voltammograms in a 0.5 M H₂SO₄ electrolyte at a scan rate of 50 mV s^{–1}. (b) Specific ECSA values. (c) Cyclic voltammograms in a 2 M CH₃OH and 0.5 M H₂SO₄ electrolyte at a scan rate of 50 mV s^{–1}. The inset shows the onset potentials in the forward scan. (d) Anodic current densities and I_F/I_B ratios of the five electrocatalysts.

available active sites. Pt/Ru–RuO₂ 400 has the largest ECSA because the nanosized Pt catalyst particles are well dispersed on the porous, nanosized grains of the support material.

To determine the electrocatalytic activity of the composites, CV measurements for the MOR were performed in a 2 M CH₃OH and 0.5 M H₂SO₄ electrolyte between –0.2 and 1.0 V (vs. Ag/AgCl) at a scan rate of 50 mV s^{–1} and normalized by the Pt loading mass, as shown in Fig. 5c. In general, the MOR at the electrode produces six electrons, six protons, and carbon dioxide (CH₃OH + H₂O → 6e[–] + 6H⁺ + CO₂).^{12–14} All CV curves exhibit a typical methanol oxidation peak in the forward scan and a typical oxidation peak for intermediate carbonaceous species such as CO, COOH, and CHO (mainly CO) in the backward scan.^{12,13} The electrochemical properties of commercial Pt/C, Pt/Ru–CNFs, Pt/Ru–RuO₂ 300, Pt/Ru–RuO₂ 400, and Pt/Ru–RuO₂ 500, such as onset potential, anodic current density, and ratio of the forward peak current (*I_F*) to the backward peak current (*I_B*), are summarized in Table 1. It is well known that Pt electrocatalysts tend to adsorb CO on their surfaces, resulting in higher onset potentials and lower electrocatalytic activity. However, Pt/Ru–RuO₂ 400 has the lowest onset potential of 533 mV (inset in Fig. 5c) compared with the other samples. This result is ascribed to the lower activation energy needed to cause methanol oxidation because of the easier removal of the adsorbed CO during the catalytic process.^{10,11,50} This result indicates that Pt/Ru–RuO₂ 400 has excellent CO tolerance, leading to improved reaction kinetics. The anodic current density (Fig. 5d) of Pt/Ru–RuO₂ 400 in the forward scan at 0.65 V is 641.7 mA mg_{Pt}^{–1}, which is 3.4, 4.4, 1.5, and 2.2 times higher than that of commercial Pt/C, Pt/Ru–CNFs, Pt/Ru–RuO₂ 300, and Pt/Ru–RuO₂ 500, respectively. Furthermore, Pt/Ru–RuO₂ 400 exhibits the highest electrocatalytic activity in the MOR, owing to the well-dispersed Pt catalyst on the supports, which leads to an increased contact area between the Pt catalyst and the electrolyte. It is well known that the *I_F*/*I_B* ratio can be used to demonstrate the CO tolerance of the catalyst surface during the MOR, as shown in Fig. 5d. The *I_F*/*I_B* ratio for Pt/Ru–RuO₂ 400 is 1.9, indicating the highest CO tolerance among the samples. The improved CO tolerance can be explained by the bifunctional effect (Ru–OH + Pt–CO → Pt + Ru + CO₂ + H⁺ + e[–]).^{7,12,20} Furthermore, the existence of metallic Ru atoms on the support surface facilitates removal of adsorbed CO species at low potential by the abundant adsorbed hydroxyl species, resulting in clean active sites on the Pt catalyst and improved electrocatalytic activity in the MOR.^{21,36} Thus, the improved electrochemical activity of Pt/Ru–RuO₂ 400 can be attributed to the well-dispersed Pt catalyst and

Table 1 Onset potential, anodic current density, and ratio of the forward peak current (*I_F*) to the backward peak current (*I_B*) for commercial Pt/C, Pt/Ru–CNFs, Pt/Ru–RuO₂ 300, Pt/Ru–RuO₂ 400, and Pt/Ru–RuO₂ 500

Samples	Onset potential (mV)	Anodic current density (mA mg _{Pt} ^{–1}) at 0.65 V	<i>I_F</i> / <i>I_B</i> ratio
Pt/C	1347	188.4	0.6
Pt/Ru–CNFs	1846	143.1	0.8
Pt/Ru–RuO ₂ 300	970	416.7	1.5
Pt/Ru–RuO ₂ 400	533	641.7	1.9
Pt/Ru–RuO ₂ 500	750	281.5	1.3

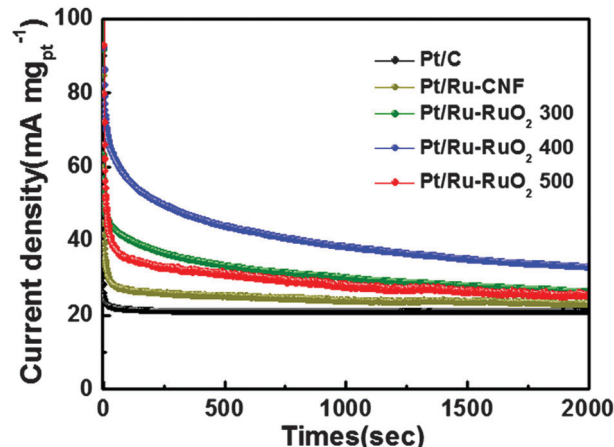


Fig. 6 Chronoamperometry curves of commercial Pt/C, Pt/Ru–CNFs, Pt/Ru–RuO₂ 300, Pt/Ru–RuO₂ 400, and Pt/Ru–RuO₂ 500 in a 2 M CH₃OH and 0.5 M H₂SO₄ electrolyte at a constant potential of 0.5 V for 2000 s.

the bifunctional effect that manifests when supports containing metallic Ru are used. However, Pt/Ru–RuO₂ 500 exhibits lower electrocatalytic activity because of the dense agglomeration of the Pt catalyst (Fig. 2h and 3h).

The improvement in catalyst stability is one of the most important factors for DMFC development. Thus, the electrocatalytic stability of the samples was investigated by CA measurements in a 2 M CH₃OH and 0.5 M H₂SO₄ electrolyte at a constant potential of 0.5 V for 2000 s, as shown in Fig. 6. Current decay was observed during the MOR for all samples because of the adsorption of intermediate carbonaceous species and SO₄^{2–} anions onto the Pt catalyst surface.^{9,18,21,23} Nevertheless, Pt/Ru–RuO₂ 400 indicates the highest current density and the lowest deterioration rate, indicating its superior stability and CO tolerance compared to that of the other samples, which is due to the well-dispersed Pt catalyst and the bifunctional effect of the metallic Ru in the support.

Novel architectures like Pt/Ru–RuO₂ 400 exhibit improved electrochemical performance in the MOR for three major reasons

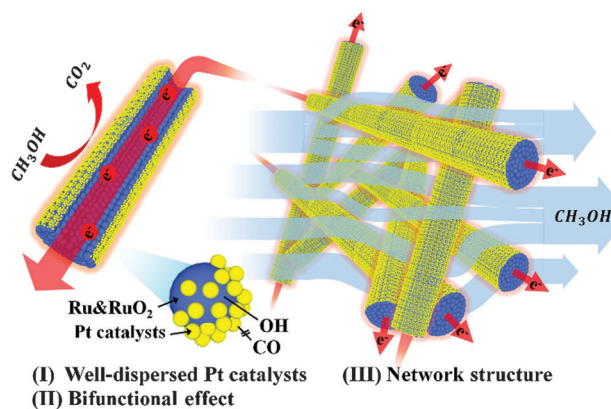


Fig. 7 Schematic representation of the advantages of Pt/Ru–RuO₂ 400, including the well-dispersed Pt catalyst on the support, the bifunctional effect, and the interconnected network structure of the support.

(Fig. 7). First, the well-dispersed Pt catalyst on the support provides an increased contact area between the Pt catalyst and the electrolyte, thus increasing the anodic current density during the MOR. Second, the existence of Ru atoms on the support surfaces substantially improves CO tolerance through the bifunctional effect, leading to low onset potential and improved electrocatalytic stability. Finally, the network structure of the support allows for efficient electron transfer and a rapid rate of electrolyte diffusion during the MOR. Pt/Ru–RuO₂ 400 exhibits a combination of all these advantages, and therefore has excellent potential as a novel catalyst for high-performance DMFCs.

Conclusions

Ru and RuO₂ nanofiber support/Pt catalyst composites arranged into nanosized grains were fabricated by electrospinning, post-calcination, and reduction. Pt/Ru–RuO₂ 400 exhibited improved electrochemical activity with the lowest onset potential of 533 mV, the highest anodic current density of 641.7 mA mg_{Pt}⁻¹, the highest I_F/I_B ratio of 1.9, and excellent electrocatalytic stability compared to commercial Pt/C, Pt/Ru–CNFs, Pt/Ru–RuO₂ 300, and Pt/Ru–RuO₂ 500. The excellent electrochemical activity and stability of Pt/Ru–RuO₂ 400 can be explained in terms of three major factors: (I) its high anodic current density is related to the Pt catalyst being well dispersed on the nanosized grains of the porous support; (II) its low onset potential, high I_F/I_B ratio, and excellent electrocatalytic stability are related to the existence of Ru atoms on the support surface, which promote the bifunctional effect; and (III) its efficient electron transfer and rapid rate of electrolyte diffusion are related to the unique network structure of the support material. Accordingly, we believe that this novel Ru and RuO₂ nanofiber material consisting of nanosized grains can be used as a Pt catalyst support, offering a new strategy for high-performance DMFCs.

Acknowledgements

This work was supported by the International Collaborative Energy Technology R&D Program of the Korea Institute of Energy Technology Evaluation and Planning (KETEP), and was granted financial support from the Ministry of Trade, Industry & Energy, Republic of Korea (No. 20138520030800).

References

- B. C. H. Steele and A. Heinzl, *Nature*, 2001, **414**, 345–352.
- M. K. Debe, *Nature*, 2012, **486**, 43–51.
- X. Shan, I. Díez-Pérez, L. Wang, P. Wiktor, Y. Gu, L. Zhang, W. Wang, J. Lu, S. Wang, Q. Gong, J. Li and N. Tao, *Nat. Nanotechnol.*, 2012, **7**, 668–672.
- N. Kakati, J. Maiti, S. H. Lee, S. H. Jee, B. Viswanathan and Y. S. Yoon, *Chem. Rev.*, 2014, **114**, 12397–12429.
- A. S. Aricò, P. Bruce, B. Scrosati, J.-M. Tarascon and W. Schalkwijk, *Nat. Mater.*, 2005, **4**, 366–377.
- A. Chen and P. Holt-Hindle, *Chem. Rev.*, 2010, **110**, 3767–3804.
- A. E. Russell and A. Rose, *Chem. Rev.*, 2004, **104**, 4613–4635.
- H. Atae-Esfahani, L. Wang, Y. Nemoto and Y. Yamauchi, *Chem. Mater.*, 2010, **22**, 6310–6318.
- G.-H. An and H.-J. Ahn, *J. Electroanal. Chem.*, 2013, **707**, 74–77.
- T.-Y. Chen, H. D. Li, G.-W. Lee, P.-C. Huang, P.-W. Yang, Y.-T. Liu, Y.-F. Liao, H.-T. Jeng, D.-S. Lin and T.-L. Lin, *Phys. Chem. Chem. Phys.*, 2015, **17**, 15131–15139.
- Y. Ma, R. Wang, H. Wang, V. Linkov and S. Ji, *Phys. Chem. Chem. Phys.*, 2014, **16**, 3593–3602.
- X. Zhao, M. Yin, L. Ma, L. Liang, C. Liu, J. Liao, T. Lu and W. Xing, *Energy Environ. Sci.*, 2011, **4**, 2736–2753.
- H. Liu, C. Song, L. Zhang, J. Zhang, H. Wang and D. P. Wilkinson, *J. Power Sources*, 2006, **155**, 95–110.
- X. Li and A. Faghri, *J. Power Sources*, 2013, **226**, 223–240.
- P. Gnanaprakasam, S. E. Jeena and T. Selvaraju, *J. Mater. Chem. A*, 2015, **3**, 18010–18018.
- S. Basri, S. K. Kamarudin, W. R. W. Daud and Z. Yaakub, *Int. J. Hydrogen Energy*, 2010, **35**, 7957–7970.
- S. K. Kamarudin and N. Hashim, *Renewable Sustainable Energy Rev.*, 2012, **16**, 2494–2515.
- L. Wang, L. Zhao, P. Yu, C. Tian, F. Sun, H. Feng, W. Zhou, J. Wang and H. Fu, *J. Mater. Chem. A*, 2015, **3**, 24139–24147.
- L. Nan, W. Yue and Y. Jiang, *J. Mater. Chem. A*, 2015, **3**, 22170–22175.
- H. Huang, G. Ye, S. Yang, H. Fei, C. S. Tiwary, Y. Gong, R. Vajtal, J. M. Tour, X. Wang and P. M. Ajayan, *J. Mater. Chem. A*, 2015, **3**, 19696–19701.
- Y. Ding, B. Jin, G. Gu and X.-H. Xia, *J. Mater. Chem.*, 2009, **19**, 9141–9146.
- S. Şen, F. Şen and G. Gökçağaç, *Phys. Chem. Chem. Phys.*, 2011, **13**, 6784–6792.
- G.-H. An and H.-J. Ahn, *ECS Solid State Lett.*, 2014, **3**, M29–M32.
- S. Sharma and B. G. Pollet, *J. Power Sources*, 2012, **208**, 96–119.
- H. Liu, Y. Feng, D. Chen, C. Li, P. Cui and J. Yang, *J. Mater. Chem. A*, 2015, **3**, 3182–3223.
- H. L. An, G.-H. An and H.-J. Ahn, *J. Alloys Compd.*, 2015, **645**, 317–321.
- H. Lv, N. Cheng, T. Peng, M. Pan and S. Mu, *J. Mater. Chem.*, 2012, **22**, 1135–1141.
- Y. Ito, T. Takeuchi, T. Tsujiguchi, M. A. Abdelkareem and N. Nakagawa, *J. Power Sources*, 2013, **242**, 280–288.
- S. Yu, Q. Liu, W. Yang, K. Han, Z. Wang and H. Zhu, *Electrochim. Acta*, 2013, **94**, 245–251.
- H. L. Pang, X. H. Zhang, X. X. Zhong, B. Liu, X. G. Wei, Y. F. Kuang and J. H. Chen, *J. Colloid Interface Sci.*, 2008, **319**, 193–198.
- W.-Z. Hung, W.-H. Chung, D.-S. Tsai, D. P. Wilkinson and Y.-S. Huang, *Electrochim. Acta*, 2010, **55**, 2116–2122.
- Y. Fan, J. Liu, H. Lu, P. Huang and D. Xu, *Electrochim. Acta*, 2012, **76**, 475–479.
- K. Yamaguchi, J. W. Kim, J. He and N. Mizuno, *J. Catal.*, 2009, **268**, 343–349.
- F. Peng, C. Zhou, H. Wang, H. Yu, J. Liang and J. Yang, *Catal. Commun.*, 2009, **10**, 533–537.

- 35 F. Scheiba, M. Scholz, L. Cao, R. Schafrank, C. Roth, C. Cremers, X. Qiu, U. Stimming and H. Fuess, *Fuel Cells*, 2006, **6**, 439–446.
- 36 H. M. Villullas, F. I. Mattos-Costa and L. O. S. Bulhões, *J. Phys. Chem. B*, 2004, **108**, 12898–12903.
- 37 Z.-M. Huang, Y.-Z. Zhang, M. Kotaki and S. Ramakrishna, *Compos. Sci. Technol.*, 2003, **63**, 2223–2253.
- 38 G.-H. An and H.-J. Ahn, *J. Power Sources*, 2014, **272**, 826–836.
- 39 Y.-J. Gu and W.-T. Wong, *J. Electrochem. Soc.*, 2006, **153**, A1714–A1718.
- 40 Y.-S. Yeom and H.-J. Ahn, *Korean J. Mater. Res.*, 2011, **21**, 419–424.
- 41 F. Zhang, C. Yuan, J. Zhu, J. Wang, X. Zhang and X. W. Lou, *Adv. Funct. Mater.*, 2013, **23**, 3909–3915.
- 42 L. Shang, T. Bian, B. Zhang, D. Zhang, L.-Z. Wu, C.-H. Tung, Y. Yin and T. Zhang, *Angew. Chem., Int. Ed.*, 2014, **53**, 250–254.
- 43 A. Baldan, *J. Mater. Sci.*, 2002, **37**, 2171–2202.
- 44 M. E. Scofield, C. Koenigsmann, L. Wnag, H. Liu and S. S. Wong, *Energy Environ. Sci.*, 2015, **8**, 350–363.
- 45 Y. Sun, C. Du, M. An, L. Du, Q. Tan, C. Liu, Y. Gao and G. Yin, *J. Power Sources*, 2015, **300**, 245–253.
- 46 G.-H. An and H.-J. Ahn, *J. Electroanal. Chem.*, 2015, **744**, 32–36.
- 47 G.-H. An, H.-J. Ahn and W.-K. Hong, *J. Power Sources*, 2015, **274**, 536–541.
- 48 A. Pozio, M. D. Francesso, A. Cemmi, F. Cardellini and L. Giorgi, *J. Power Sources*, 2002, **105**, 13–19.
- 49 S.-H. Ye, J.-X. Feng, A.-L. Wang, H. Xu and G.-R. Li, *J. Mater. Chem. A*, 2015, **3**, 23201–23206.
- 50 V. T. T. Ho, N. G. Nguyen, C.-J. Pan, J.-H. Cheng, J. Rick, W.-N. Su, J.-F. Lee, H.-S. Sheu and B.-J. Hwang, *Nano Energy*, 2012, **1**, 687–695.